A Matrix Presentation of State-Plane Analysis for a Broad Class of Series-Resonant Converters

Davide Biadene, *Student Member, IEEE* and Giorgio Spiazzi, *Member, IEEE*

***Abstract*—The trend toward higher switching frequencies and higher power densities in dc–dc conversion led the designers to rediscover resonant topologies. However, the analysis of these converters is often limited to a particular operating mode and/or topology. This paper wants to fill the gap by presenting a state-space-based analysis for a broad class of series-resonant converters including voltage-fed as well as current-fed topologies, either unidirectional or bidirectional. The proposed solution consists of a mathematical framework that solves the trajectory of state variables in the resonant tank, as well as the main characteristic functions such as voltage conversion ratio and transferred power. The matrix approach permits a flexible and compact formulation and easy implementation in computational tools such as MATLAB. The theoretical framework is applied to both voltage-fed and current-fed resonant topologies: the first is used to show the advantages of the proposed model respect to the first harmonic approximation, while a detailed analysis in terms of operating mode boundaries, delivered power, and voltage gain is provided for the second. Simulations and measurements on a 300-W prototype of the current-fed topology are used to validate the correctness of the proposed solution.**

***Index Terms*—DC-DC converters, resonant converters, state-space methods, time-domain analysis.**

I. Introduction

A BROAD class of dc–dc converters is based on an energy transfer mechanism that involves the use of a current shaping impedance inserted between two equivalent voltage sources, as represented in Fig. 1. In many cases, the current shaping impedance is a simple inductor, like in the unidirectional single-active-bridge topology [1] or in the more popular bidirectional dual-active-bridge (DAB) converter [2]–[9]. The same energy transfer mechanism is found also in current-fed topologies, such as in [10]–[14], and in their bidirectional counterpart [15]–[17]. In fact, in these topologies, despite the use of input-port inductors, internal clamp capacitors act as voltage sources that generate the voltage $v_A(t)$ in Fig. 1.

In unidirectional topologies, voltage $v_A(t)$ is imposed by the modulation algorithm, while voltage $v_B(t)$ is related to the inductor current sign through the action of the rectification circuits in the switching network Sw_2, while in bidirectional topologies, both voltages $v_A(t)$ and $v_B(t)$ are determined by the control algorithm. In any case, a stair-case voltage $v_Z(t) = v_A(t) - v_B(t)$ is produced, with a consequent piecewise linear inductor current waveform.

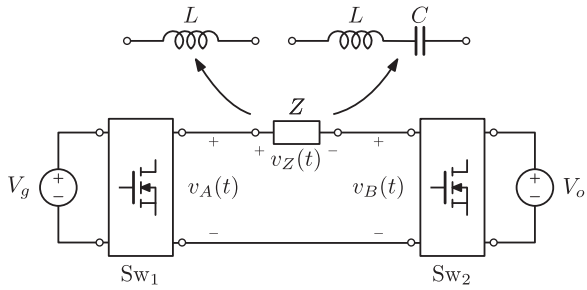

Fig. 1. Generalized dc–dc conversion involving a current shaping impedance.

All aforementioned converters can be modified to obtain a resonant behavior by using a series-resonant (SR) *LC* tank as current shaping impedance in Fig. 1. In some cases, the series capacitor is used just as dc blocking element to prevent core saturation in isolated topologies, thus not modifying the piecewise linear inductor current waveform. In many other situations, the resonant behavior is exploited to improve the soft-switching conditions of both switches and/or diodes or to allow higher operation frequency with reduced electromagnetic interferences, thus allowing to develop high-efficiency and high-power-density dc–dc converters. This is the case of the resonant DAB topologies [18]– [28], and their corresponding current-fed counterpart [29]–[33].

In most of the papers presented in the literature, the steady-state analysis of the SR converter is worked out using either brute-force simulation or two well-known mathematical frameworks: the fundamental harmonic approximation (FHA) as done in [18]–[22] and [27], where the voltages $v_A(t)$ and $v_B(t)$ are approximated with their components at the switching frequency [34], or the state-plane (normalized) analysis (SPA) as done in [23]–[30], where the ordinary differential equations (ODEs) of the resonant tank are solved. The brute-force simulation method allows one to explore the characteristic functions, e.g., voltage conversion ratio, of the under-test topology sampling the space of the control variables. In this way, to attain high-resolution characteristics, a large number of simulations have to be carried out with a huge time consumption. On the contrary, the FHA

Manuscript received July 14, 2017; revised October 11, 2017 and December 15, 2017; accepted January 31, 2018. Date of publication February 16, 2018; date of current version September 28, 2018. Recommended for publication by Associate Editor S. Kapat. *(Corresponding author: Davide Biadene.)*

D. Biadene is with the Department of Information Engineering, University of Padova, and is also with the Interdepartmental Centre Giorgio Levi Cases, University of Padova, 35122 Padova, Italy (e-mail: davide.biadene@dei.unipd.it).

G. Spiazzi is with the Department of Information Engineering, University of Padova, 35122 Padova, Italy (e-mail: giorgio.spiazzi@dei.unipd.it).

Color versions of one or more of the figures in this paper are available online at http://ieeexplore.ieee.org.

Digital Object Identifier 10.1109/TPEL.2018.2806915

TABLE I
BASE AND NORMALIZED VARIABLE DEFINITIONS

Variable	Base	Normalized
Impedance/load	$Z_r = \sqrt{\frac{L}{C}}$	$\rho = \frac{R}{Z_r}$
Frequency	$f_r = \frac{1}{2\pi\sqrt{LC}}$	$F = \frac{f_{sw}}{f_r}$
Voltage	$V_{\text{base}} = V_o$	$u_x = \frac{v_x}{V_{\text{base}}}$
Current	$I_{\text{base}} = \frac{V_{\text{base}}}{Z_r}$	$j_x = \frac{i_x}{I_{\text{base}}}$
Power	$P_{\text{base}} = \frac{V_{\text{base}}^2}{Z_r}$	$\Gamma_x = \frac{P_x}{P_{\text{base}}}$

approach permits a fast analysis providing closed-form equations of the circuit, but the accuracy is markedly reduced based on the made approximation. Finally, the SPA describes exactly the topology behavior with the resultant equations but requires a greater calculation effort that represents its bottleneck.

The work presented in this paper is aimed to provide a mathematical framework to figure out the single-resonance SPA of a broad SR converter class. Thanks to the matrix formulation, its implementation in popular mathematical tools like MATLAB is straightforward opening up to matrix calculus opportunities, e.g., optimization problems. In this way, the interested quantities in the SR converter design are obtained with a drastically reduction of time consumption. This framework highly simplifies the analytic way to study the state evolution during the commutation instants, useful for zero-voltage-switching (ZVS) and zero-current-switching (ZCS) conditions check, and to define a standard approach for the resolution of a broad class of SR converters where the energy transfer process occurs, as illustrated in Fig. 1. The rest of this paper is structured as follows. In Section II, the matrix presentation of state-plane analysis (MSPA) is described providing the main characteristic functions in typical applications. In Section III, a voltage-fed converter is taken into account providing a first example of application and highlighting the different outcomes of MSPA, SPA, FHA, and simulation approaches. Finally, in Section IV, a current-fed topology is considered in detail the aforesaid framework. The same topology was studied in [26] and [27] presenting the SPA only regards the above resonant operations. In this section, MSPA is performed extending the analysis independently of above/below resonant operation and the input/output stage implementations and providing a thorough guideline to apply the MSPA in case the converter shows more continuous conduction modes (CCMs) and discontinuous conduction modes (DCMs). The analysis is supported by simulations and experimental measurements taken on a prototype to validate the theoretical analysis.

II. MATRIX STATE-PLANE ANALYSIS

The analysis will be presented in normalized form using the base variables indicated in Table I. This approach allows one to spread its application across different topologies, where the energy exchange process takes essentially place, as illustrated in Fig. 1. The only assumption is to have stair-case voltages $v_A(t)$ and $v_B(t)$, i.e., voltage $v_Z(t)$ is constant in every switching subinterval.

A. Sampled Steady-State Trajectories

Let us suppose that the converter assumes a fixed number of topological states in the switching period T_{sw}, each associated with a given impressed voltage $V_{Z,i} = v_{A,i} - v_{B,i}$, $i \in \mathbb{N}$ and with the corresponding subinterval duration. In the ith state, the trajectory of state-space variables $(i_L\ v_C)$ is obtained resolving the ODE system imposing the initial conditions $(I_{L,i-1}\ V_{C,i-1})$ and the related voltage $V_{Z,i}$. The solution is expressed by

$$\begin{aligned} i_L(t) &= I_{L,i-1}\cos(\omega_r t) - \frac{V_{C,i-1}}{Z_r}\sin(\omega_r t) + \frac{V_{Z,i}}{Z_r}\sin(\omega_r t) \\ v_C(t) &= Z_r I_{L,i-1}\sin(\omega_r t) + V_{C,i-1}\cos(\omega_r t) \\ &\quad + V_{Z,i}(1-\cos(\omega_r t)) \end{aligned} \tag{1}$$

where $\omega_r = 2\pi f_r$ and Z_r are the resonance frequency and characteristic impedance of the *LC* tank, respectively.

Moving from time to angle dependence, i.e., $\theta = 2\pi f_{\text{sw}} t$, where f_{sw} is the switching frequency, and normalizing according to Table I, the normalized final values of state variables $\mathbf{x}_i = (J_i\ U_i)$ at θ_i instants can be related to the previous one $\mathbf{x}_{i-1}$ and the applied voltage $U_{Z,i}$ as

$$\begin{bmatrix} J_i \\ U_i \end{bmatrix} = \begin{bmatrix} \cos\frac{\delta_i}{F} & -\sin\frac{\delta_i}{F} \\ \sin\frac{\delta_i}{F} & \cos\frac{\delta_i}{F} \end{bmatrix}\begin{bmatrix} J_{i-1} \\ U_{i-1} \end{bmatrix} + \begin{bmatrix} \sin\frac{\delta_i}{F} \\ 1-\cos\frac{\delta_i}{F} \end{bmatrix} U_{Z,i} \tag{2}$$

or in the matrix form

$$\mathbf{x}_i = \mathbf{M}_i \mathbf{x}_{i-1} + \mathbf{N}_i U_{Z,i} \tag{3}$$

in which $\delta_i = \theta_i - \theta_{i-1}$ represents the subinterval duration.

Starting from the initial state $\mathbf{x}_0$ and iterating (3) for N subintervals, the sampled state trajectory at the Nth commutation is obtained as

$$\mathbf{x}_N = \mathbf{M}_{N,1}\mathbf{x}_0 + \mathbf{H}[U_g \mathbf{q}_A - \mathbf{q}_B] \tag{4}$$

where the following vectors and matrices are introduced:

1) the clockwise rotation matrix $\mathbf{M}_{k,j} = \prod_j^k \mathbf{M}_i \in \mathbb{R}^{2\times 2}$;
2) the matrix $\mathbf{H} = [\mathbf{M}_{N,2}\mathbf{N}_1 \ldots \mathbf{M}_{N,i+1}\mathbf{N}_i \ldots \mathbf{N}_N] \in \mathbb{R}^{2\times N}$;
3) the vectors $\mathbf{q}_{A,B} \in \mathbb{R}^{N\times 1}$ such that $q_{A,i}V_g = v_{A,i}$ and $q_{B,i}V_o = v_{B,i}$.

The vectors $\mathbf{q}_{A,B}$ have the purpose to abstract the voltage gain of switching networks from their implementation; in this way, more topologies can be taken into account at the same time.

If the steady-state condition is verified at the Nth interval, i.e., $\mathbf{x}_N = \mathbf{x}_0$, the initial state value can be derived from (4) as

$$\mathbf{x}_0 = \mathbf{W}[U_g \mathbf{q}_A - \mathbf{q}_B] \tag{5}$$

with $\mathbf{W} = (\mathbf{I} - \mathbf{M}_{N,1})^{-1}\mathbf{H}$. The expression of the kth column vector of $\mathbf{W}$ is

$$\mathbf{w}_k = \frac{\sin\frac{\delta_k}{2F}}{\sin\frac{\delta_{N,1}}{2F}} \begin{bmatrix} -\sin\frac{\delta_{N,k}-\delta_{k,1}}{2F} \\ \cos\frac{\delta_{N,k}-\delta_{k,1}}{2F} \end{bmatrix} \tag{6}$$

where the compact angle notation $\delta_{m,n} = \sum_n^m \delta_i$ for $m > n$ or $\delta_{m,n} = \delta_{N,1} + \delta_m + \delta_n - \delta_{n,m}$ for $m < n$ is introduced. Only active topological states take part in (4) and (5), namely the intervals where the resonant tank variables do not change are

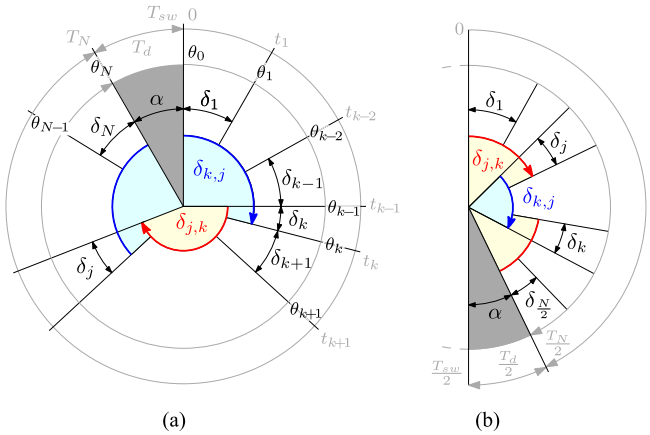

Fig. 2. Angle convention. (a) Nonsymmetrical case ($j > k$). (b) Half-wave symmetrical case ($j < k$). The time T_N is equal to the switching period $T_{\rm sw}$ for CCMs, otherwise to $T_{\rm sw} - T_d$ for DCMs, with T_d is the overall dead time, where the inductor current stays zero.

neglected. The dead time T_d, and the associated dead angle α, in the DCM is an example of a neglected interval, since the inductor current i_L stays zero and the capacitor voltage v_C is clamped during all its duration. A graphical interpretation of the just introduced angle convection is reported in Fig. 2(a). This result permits to figured out the sampled state trajectory in all operating modes, either CCM and DCM, computing (5) and proceeding along the sampled trajectory with (3).

In case the impressed voltage $u_Z(t)$ is a half-wave symmetric waveform, i.e., $\delta_k = \delta_{N/2+k}$ and $q_{A(B),k} = -q_{A(B),N/2+k}$ with $k \in [1, N/2]$, (5) can be computed using only the first $N/2$ inputs, and the renamed column vector $\mathbf{w}'_k$ of matrix $\mathbf{W}' \in \mathbb{R}^{2\times N/2}$ assumes the following expression:

$$\mathbf{w}'_k = -\frac{\sin\frac{\delta_k}{2F}}{\cos\frac{\delta_{N/2,1}}{2F}}\begin{bmatrix}\cos\frac{\delta_{N/2,k}-\delta_{k,1}}{2F}\\ \sin\frac{\delta_{N/2,k}-\delta_{k,1}}{2F}\end{bmatrix} \tag{7}$$

such that

$$\mathbf{x}_0 = \mathbf{W}'[U_g\mathbf{q}'_A - \mathbf{q}'_B] \tag{8}$$

with $\mathbf{q}'_{A,B} \in \mathbb{R}^{N/2\times 1}$ are the related subvectors of $\mathbf{q}_{A,B}$ considering only the first $N/2$ elements.

B. Normalized Output Power

The normalized output power is given by

$$\Gamma = \frac{P_o}{P_{\rm base}} = \frac{1}{2\pi}\sum_1^N q_{B,i}\int_{\delta_i} j_L(\theta)\,d\theta. \tag{9}$$

The inductor current i_L is related to the resonant capacitor voltage v_C by the normalized differential $j_L\,d\theta = F\,du_C$. Substituting this relationship in (9) gives

$$\Gamma = \frac{F}{2\pi}\sum_1^N q_{B,i}\,[U_i - U_{i-1}] = \frac{F}{2\pi}\mathbf{q}_B^T\mathbf{\Delta U} \tag{10}$$

where the vector $\mathbf{\Delta U} = [\Delta U_1\ \ldots\ \Delta U_N]^T \in \mathbb{R}^{N\times 1}$ is defined as stack of the difference between two consecutive capacitor voltage state values, i.e., $\Delta U_k = U_k - U_{k-1}$. Using (3) and (5), the vector $\mathbf{\Delta U}$ is related to the vectors $\mathbf{q}_{A,B}$ through the matrix $\mathbf{S} \in \mathbb{R}^{N\times N}$ such that

$$\mathbf{\Delta U} = \mathbf{S}[\mathbf{q}_A U_g - \mathbf{q}_B]$$

$$S_{j,k} = \frac{2\sin\frac{\delta_j}{2F}\sin\frac{\delta_k}{2F}}{\sin\frac{\delta_{N,1}}{2F}}\sin\frac{\delta_{k,j}-\delta_{j,k}}{2F}. \tag{11}$$

The matrix $\mathbf{S}$ is $N \times N$ skew-symmetric, i.e., $\mathbf{S} \in \mathrm{Skew}_N$, because $S_{j,k} = -S_{k,j}$ and $S_{j,j} = 0$. By the $\mathrm{Skew_N}$ properties, the term $\mathbf{q}_B^T\mathbf{S}\mathbf{q}_B = 0$ in (10), so that the final expression of Γ is

$$\Gamma = \frac{FU_g}{2\pi}\mathbf{q}_B^T\mathbf{S}\mathbf{q}_A. \tag{12}$$

In case of half-wave symmetry, as done in Section II-A, the value of output power becomes dependent only on the first $N/2$ intervals and the matrix $\mathbf{S}' \in \mathrm{Skew}_{N/2}$ is given for $j > k$ by

$$S'_{j,k} = \frac{4\sin\frac{\delta_j}{2F}\sin\frac{\delta_k}{2F}}{\cos\frac{\delta_{N/2,1}}{2F}}\cos\frac{\delta_{k,j}-\delta_{j,k}}{2F} \tag{13}$$

where the angle convention reported in Fig. 2(b) is used. In this case, (12) becomes

$$\Gamma = \frac{FU_g}{2\pi}\mathbf{q}_B'^T\mathbf{S}'\mathbf{q}'_A. \tag{14}$$

C. Voltage Conversion Ratio

In case of resistive load, the output power can be linked to the resistance value R_o in the following normalized form:

$$\Gamma = \frac{P_o}{P_{\rm base}} = \frac{V_o^2}{R_o}\frac{Z_r}{V_{\rm base}^2} = \frac{1}{\rho_o}. \tag{15}$$

Since (12) must be equal to (15) and U_g is the reciprocal of the voltage conversion ratio M, the latter is equal to

$$M = \frac{F\rho_o}{2\pi}\mathbf{q}_B^T\mathbf{S}\mathbf{q}_A. \tag{16}$$

This generic approach permits to study also complex topologies where the duration of the intervals or the impressed voltage is dependent on the current, for example due to the presence of a full-wave or a doubler voltage rectifier in the output side. In this case, a known condition, e.g., zero-current state, is required to solve the topological state succession in terms of duration and initial conditions. Consequence of this dependence also appears in (16) turning it into an implicit formula, since $\mathbf{S}$ becomes function of M.

In the following sections, the bidirectional phase shift modulated (PSM) SR dual half bridge (DHB) and the unidirectional interleaved boost with coupled inductors (IBCI) converters as examples are considered. The first is obtained by substituting the switching networks $\mathrm{Sw}_{1,2}$ in Fig. 1 with two half-bridge legs, as shown in Fig. 3(a), while the second topology is depicted in Fig. 6. Both converter analyses are presented using the above-mentioned method to find the closed-form input–output characteristic functions with two different focuses: the PSM DHB topology described in Section III provides a simple application example easily comparable with FHA model; and the

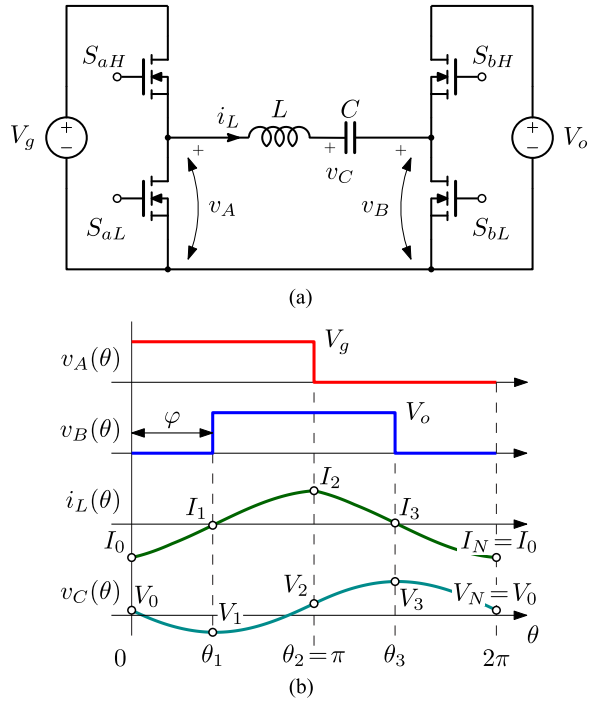

Fig. 3. Scheme and main waveforms of SR PSM DHB. (a) DHB scheme. (b) Main waveforms.

IBCI topology, on the other hand, provides a complex example, in which the CCM and the DCM are present and the boundary conditions have to be found.

III. Case Study 1: PSM SR DHB

The PSM DHB is a simple analyzable SR voltage-fed converter that is widely studied in the literature. In this section, the proposed method is first applied to briefly show its usability and then compared with the corresponding FHA model.

A. Functional Description

Both impressed voltages $v_{A,B}(\theta)$ are two-level voltage square wave owing to the switching network implementation and the modulation scheme. The power transferring is achieved, thanks to the phase shift φ between v_A and v_B voltages, which is also the control variable. The main converter waveforms are depicted in Fig. 3(b), highlighting the commutation instants θ_i and their state-space values $(I_i\, V_i)$. The following analysis is limited to $\varphi \in [0,\ \frac{\pi}{2}]$ and $F > 0.5$. For $\varphi \in [-\frac{\pi}{2},\ 0]$, the power flow reversal is obtained, but the converter operation remains the same.

B. State-Space Analysis

The PSM DHB presents only one operating mode, i.e., CCM, so no boundary conditions have to be found. The converter is characterized by four topological states, as shown in Fig. 3(b), and the corresponding definition of $\mathbf{q}_{A,B}$ vectors and their interval durations δ_i, $i \in [1, 4]$, is reported in Table II. It is worth noting that δ_i definition, as well as matrices $\mathbf{W}$ and $\mathbf{S}$, is a function of the control variable φ.

TABLE II
Definition of $\mathbf{q}_A$, $\mathbf{q}_B$, and δ_i for SR PSM DHB

i	$q_{A,i}$	$q_{B,i}$	δ_i
1	1	0	φ
2	1	1	$\pi - \varphi$
3	0	1	φ
4	0	0	$\pi - \varphi$

Using (3) and (5), the normalized expressions of $I_{0,1}$ are

$$J_0 = \frac{1}{2\cos\frac{\pi}{2F}}\left[-U_g \sin\frac{\pi}{2F} + \sin\frac{\pi - 2\varphi}{2F}\right] \tag{17a}$$

$$J_1 = \frac{1}{2\cos\frac{\pi}{2F}}\left[-U_g \sin\frac{\pi - 2\varphi}{2F} + \sin\frac{\pi}{2F}\right]. \tag{17b}$$

These expressions contain information about ZVS and ZCS conditions: the locus of points (φ, F) where (17) is zero identifies a ZCS condition, while ZVS can be evaluated studying the sign of (17) in the (φ, F) plane.

To compare the previous results with the outcomes of the FHA method, the sampled values of the current phasor at $\theta_{0,1}$ are calculated as follows:

$$J_{0,\mathrm{FHA}} = \frac{2}{\pi}\frac{F}{F^2 - 1}\left[\cos\varphi - U_g\right] \tag{18a}$$

$$J_{1,\mathrm{FHA}} = \frac{2}{\pi}\frac{F}{F^2 - 1}\left[1 - U_g\cos\varphi\right]. \tag{18b}$$

Differently from the exact analysis, (18a) never zeros for $U_g > 1$ as well as (18b) for $U_g < 1$. This information loss affects both the soft and hard switching estimation, greatly in below resonance operation, as shown in Fig. 4(a) for $U_g = 12/5$, $\varphi^* = 0.21\pi$, and $F^* = 0.58$. The FHA model in the considered scenario, i.e., $0.5 < F < 1$, provides a wrong estimation of commutated currents. The relative error $\varepsilon_{J_0} = \frac{J_{0,\mathrm{FHA}}}{J_0} - 1$ plotted in Fig. 4(b) in the $(\varphi,\ F)$ plane reveals the importance of an accurate prediction of the current at the commutation instants for a correct switching loss estimation. Once again, such an error rapidly increases entering the below resonance region.

Now, focusing on the power, the necessary elements of $\mathbf{S}$ in (12) are the set of $S_{j,k}$ such that $j \neq k$, $q_{A,k} \neq 0$ and $q_{B,j} \neq 0$ since $q_{B,j}\, S_{j,k}\, q_{A,k} = 0$ for the others. Then, the useful matrix elements are

$$S_{2,1} = S_{3,2} = \frac{\sin\frac{\varphi}{2F}\sin\frac{\pi-\varphi}{2F}}{\cos\frac{\pi}{2F}}, \quad S_{3,1} = 0 \tag{19}$$

that provide the normalized output power Γ equation through (12) as

$$\Gamma = \frac{F}{\pi}U_g\ \frac{\sin\frac{\varphi}{2F}\sin\frac{\pi-\varphi}{2F}}{\cos\frac{\pi}{2F}}. \tag{20}$$

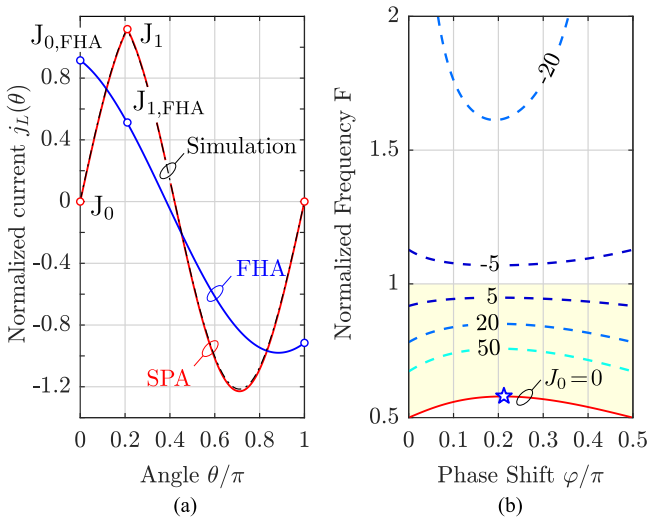

Fig. 4. Comparison between FHA, SPA, and MSPA models and simulation. (a) Normalized current waveforms in a semiperiod at $U_g = 12/5$, $\varphi^* = 0.21\pi$, and $F^* = 0.58$. For $\theta \in [\pi,\ 2\pi]$, the currents are equal to $-j_L(\theta - \pi)$. (b) Percentage relative error ε_{J_0} (isolines) between (17a) and (18a) as a function of F and φ at $U_g = 12/5$. The red line represents the points satisfying $J_0 = 0$, where the point $(\varphi^*,\ F^*)$ is highlighted. The yellow area indicates the region of positive values for J_0.

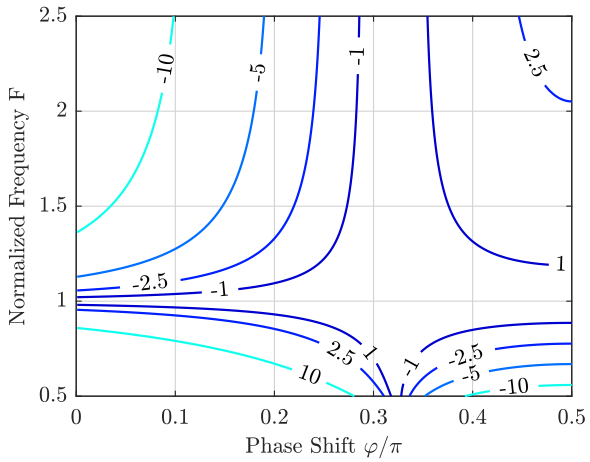

Fig. 5. Percentage relative error between (21) and (20), i.e., $\epsilon_{r\%} = 100(\frac{\Gamma_{\text{FHA}}}{\Gamma} - 1)$, as a function of the normalized frequency F and the phase shift angle φ.

Performing the FHA analysis, the normalized output power Γ_{FHA} is given by

$$\Gamma_{\text{FHA}} = \frac{2}{\pi^2} U_g \frac{F}{F^2 - 1} \sin\varphi. \tag{21}$$

The discrepancy between (20) and (21) is plotted in Fig. 5 in terms of percentage relative error as a function of the normalized frequency F and the normalized phase shift angle $\frac{\varphi}{\pi}$. As shown in Fig. 5, the closer operating point $(\varphi,\ F)$ gets to the axes, the more discrepancy is between the two approaches surpassing even the 10% in magnitude.

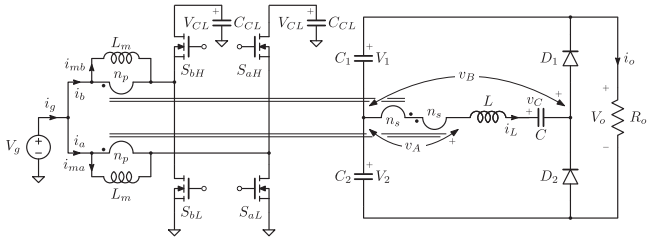

Fig. 6. IBCI: the impressed voltages $v_{A,B}$ are highlighted, as well as the state-space variables $(i_L\ v_C)$, respectively, the current through the total leakage inductor L and the resonant capacitor voltage C.

IV. Case Study 2: IBCI

The IBCI topology reported in Fig. 6 belongs to the current-fed converter family cited in the introduction and has been previously studied in [11] and [27], [35], where the analysis was figured out in the nonresonant and above-resonance case, respectively. The coexistence of both the CCM and the DCM in the said unidirectional topology requires to find the related boundary conditions needing a further step in the analysis. In this section, the survey has been extended in the below-resonance mode validating the previous solving method, providing a guideline to help the reader in the analysis steps.

A. Functional Description

The IBCI converter transfers the energy between the input and output ports through the *LC* series impedance composed of the total leakage inductance L of the mutual inductors and the resonant capacitance C, both indicated in Fig. 6. Considering a negligible voltage ripple across the clamp and output capacitors, C_{CL} and $C_{1,2}$, the converter works like the equivalent circuit of Fig. 1. The impressed voltage $v_A(\theta)$ is a three-level voltage waveform given by the two series-connected secondary windings (see Fig. 7). Due to the interleaved operation, the positive (and negative) pulse duration β is a symmetrical function of the duty cycle D, which is the control variable, around $D = 0.5$

$$\beta = \begin{cases} 2\pi D. & \text{when } D \le 0.5 \\ 2\pi(1 - D). & \text{when } D > 0.5. \end{cases} \tag{22}$$

The *volt–second* balance across each magnetizing inductance L_m yields the clamp capacitor voltage V_{CL}, which is reflected to the transformer secondary side returning the peak amplitude V_A as

$$V_A = \frac{V_g}{n(1 - D)} \tag{23}$$

where $n = n_p/n_s$ is the turn ratio of each coupled inductor.

Instead, the voltage $v_B(\theta)$ is a two-level waveform (CCM operation), whose peak amplitude V_B is equal to either half output voltage, using a voltage doubler rectifier like in Fig. 6, or the whole output voltage, when a standard full-wave rectifier is used. In order to account for both cases, the voltage gain parameter $G \in \{0.5,\ 1\}$ is introduced; therefore, $V_B = GV_o$ in the general case. Clearly, if a different rectifier stage is used like in [14], G will assume a different value (in this case 0.25).

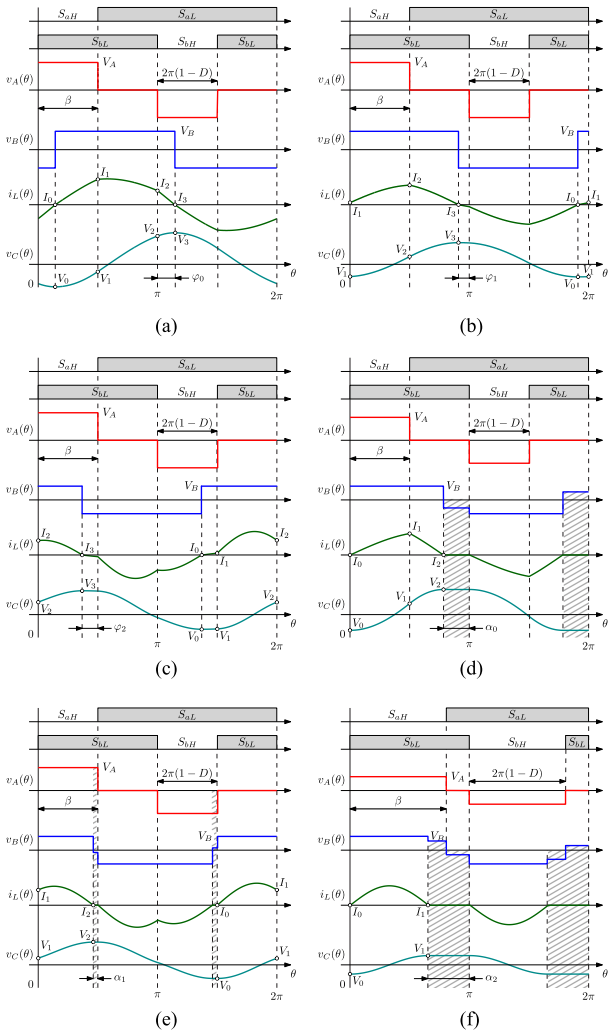

Fig. 7. Main converter waveforms in different CCM and DCM operation modes for $D > 0.5$. The waveforms related to $D < 0.5$ case are just scaled replicas of those obtained for $D > 0.5$. The gray-filled intervals will not be considered in the DCM analysis. (a) CCM_0. (b) CCM_1. (c) CCM_2. (d) DCM_0. (e) DCM_1. (f) DCM_2.

The condition $V_A \geq V_B$ is necessary to obtain a positive energy transfer from source to load.

B. State-Space Analysis

Since the IBCI converter presents a half-wave symmetry in the impressed voltage waveforms, only a semiperiod needs to be taken into account in the analysis using the angle convention illustrated in Fig. 2(b). Limiting the study for $F > 0.5$ and for the operating modes in which the inductor current i_L changes sign only one time in a switching period, the IBCI converter shows three CCMs and three DCMs reported as CCM_i and DCM_i $(i = 0, 1, 2)$ in Fig. 7 for $D > 0.5$. For CCMs, the considered number of intervals is $N/2 = 3$, while for DCMs, $N/2 = 2$ for $\text{DCM}_{0,1}$ and $N/2 = 1$ for DCM_2, since only active states are considered, i.e., the subintervals where the inductor current remains zero are ignored (see Fig. 7).

For any operating mode, the initial state $\mathbf{x}_0$ is set at the instant the inductor current i_L starts rising above zero. As a consequence, the current is always positive in the considered half switching period, as well as the impressed voltage $\mathbf{q}'_B = G\mathbf{1}$ with $\mathbf{1} = [1 \ldots 1]^T$. This choice permits a further simplification in (14) because $\mathbf{1}^T \mathbf{S}' = -4\mathbf{C_2}^T \mathbf{W}'$ with $\mathbf{C}_2 = [0\,1]^T$ giving

$$\Gamma = -\frac{2FG}{\pi} U_g \mathbf{C}_2^T \mathbf{W}' \mathbf{q}'_A \tag{24}$$

and exploiting the condition $\mathbf{C}_2^T \mathbf{W}' \mathbf{1} = 0$

$$\begin{aligned} \Gamma &= -\frac{2FG}{\pi} \mathbf{C}_2^T \mathbf{W}' \left[\mathbf{q}'_A U_g - G\mathbf{1}\right] \\ &= -\frac{2FG}{\pi} \mathbf{C}_2^T \mathbf{x}_0 = -\frac{2FG}{\pi} U_0. \end{aligned} \tag{25}$$

This result can be traced easily back to (10), where the summation is simplified as $\sum_i (U_i - U_{i-1}) = U_{N/2} - U_0 = -2U_0$. With the same tricks, the voltage gain M reported in (16) becomes

$$M = -\frac{2FG\rho_o}{\pi} \mathbf{C}_2^T \mathbf{W}' \mathbf{q}'_A. \tag{26}$$

The hereunder analysis guideline explains how to reach the closed-form expressions of normalized output power Γ, voltage conversion ratio M and the operating boundaries for the CCM_1 mode, depicted in Fig. 7(b). The same procedure has been applied to the other operating modes, paying particular attention to DCMs as described afterwards.

1) *Identify the topological state sequence* in the form of the applied voltage u_Z, thus defining the $\mathbf{q}'_{A,B}$ vectors and relative angles δ_i, as reported in Table III. The unknown angle φ_1 is introduced as the phase shift between the positive-pulse rising edges of voltages v_A and v_B, as depicted in Fig. 7(b). It is worth to highlight that δ_i are function of the control variable β and the current-sign dependent variable φ_1. For the sake of readability, the dimensionless factor λ is introduced as

$$\lambda = \frac{1}{nG(1-D)} \tag{27}$$

and (5) provides the initial state $\mathbf{x}_0$:

$$J_0 = \frac{G}{\cos\frac{\pi}{2F}} \left[\sin\frac{\pi}{2F} - \lambda U_g \sin\frac{\beta}{2F} \cos\frac{\pi-\beta-2\varphi_1}{2F}\right] \tag{28a}$$

$$U_0 = -\frac{G\lambda U_g}{\cos\frac{\pi}{2F}} \sin\frac{\beta}{2F} \sin\frac{\pi-\beta-2\varphi_1}{2F}. \tag{28b}$$

2) *Find the CCM (or DCM) Condition*. For CCMs, at the instant $\theta_{N/2}$, the inductor current i_L changes sign and starts

TABLE III
DEFINITION OF $\mathbf{q}'_A$, $\mathbf{q}'_B$, AND δ_i FOR THE CCM_1 MODE

i	$q'_{A,i}$	$q'_{B,i}$	δ_i
1	0	G	φ_1
2	$G\lambda$	G	β
3	0	G	$\pi - \beta - \varphi_1$

to flow through diode D_2 changing the u_B voltage polarity. For CCM operation, it is necessary that the inductor voltage v_L is negative in the right neighborhood of $\theta_{N/2}$, i.e., $u_L(\theta^+_{N/2}) = U_{Z,N/2+1} - U_{N/2} < 0$; otherwise, the current will be null in the next topological state (DCM case). Due to the half-wave symmetry, the same condition can be reflected to the initial state $\mathbf{x}_0$, just reversing the voltage polarities, giving

$$U_{Z,1} - U_0 > 0 \quad \rightarrow \quad U_g q'_{A,1} - U_0 > q'_{B,1} \tag{29}$$

and in the particular CCM$_1$ case for which $q'_{A,1} = 0$:

$$-U_0 > G. \tag{30}$$

3) *Extract the unknown angle* φ_1. In CCM$_1$ case, imposing (28a) equal to zero and rearranging (28b), the cosine (31a) and sine (31b) of the same angle, a function of φ_1, are obtained as

$$\cos\frac{\pi-\beta-2\varphi_1}{2F} = \frac{1}{\lambda U_g}\frac{\sin\frac{\pi}{2F}}{\sin\frac{\beta}{2F}} \tag{31a}$$

$$\sin\frac{\pi-\beta-2\varphi_1}{2F} = -\frac{U_0}{G\lambda U_g}\frac{\cos\frac{\pi}{2F}}{\sin\frac{\beta}{2F}}. \tag{31b}$$

Equation (31a) is always positive; on the other hand, (31b) is positive for $F > 1$ and negative for $F \in [\frac{1}{2}, 1]$ due to the right-side cosine term and the negative value of U_0 derived from (30). Consequently, (31) represents an angle that lies on the I or IV quadrant, which is translated in the $\mp$ sign in the following φ_1 expression:

$$\varphi_1 = \frac{\pi-\beta}{2} \mp F\arccos\left(\frac{1}{\lambda U_g}\frac{\sin\frac{\pi}{2F}}{\sin\frac{\beta}{2F}}\right). \tag{32}$$

4) *Find the feasible operating region* constraining each interval to be positive and lower than half resonant period, i.e.:

$$0 < \delta_i < \pi F, \quad i \in [1, N/2]. \tag{33}$$

The lower limit is obvious, while the upper limit is necessary to eliminate the solutions where output impressed voltage $\mathbf{q}'_B$ is incoherent with the inductor current sign because a further zero-crossing takes place. The limit case is the DCM$_2$ mode where the unique active interval lasts a resonant semiperiod, i.e., πF, and the inductor current performs a complete semicycle as depicted in Fig. 7(f) and described in detail afterwards. In the considered case (see Table III), the most restrictive inequalities obtained from (33) are

$$\beta < \pi F \tag{34a}$$

$$\varphi_1 < \pi F \tag{34b}$$

$$0 < \varphi_1 < \pi - \beta. \tag{34c}$$

Equation (34a) just identifies a semiplane in the (F, β) plane, while (34b) and (34c) must be separately discussed for $0.5 < F < 1$ and $F > 1$ because of the different definition of φ_1 in (32).

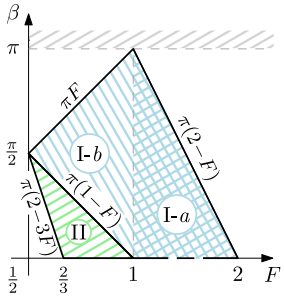

Region	Quadr.	λU_g Constraint (30)	λU_g Constraint (34b) (34c)
I-a	I	$> \lambda_1$	$< \lambda_0$
I-b	IV		
II	IV	$> \lambda_1$	$< -\lambda_0$

Fig. 8. CCM$_1$ operating region: in the table, the constraints given by the reported inequalities expressed in function of λU_g and the quadrant of the angle in (31) are highlighted.

For $0.5 < F < 1$, the lower limit in (34c) does not provide any restriction; on the other hand, the upper limit returns the following inequality:

$$\frac{1}{\lambda U_g}\frac{\sin\frac{\pi}{2F}}{\sin\frac{\beta}{2F}} > \cos\frac{\pi-\beta}{2F}. \tag{35}$$

The left-side term is always positive in the considered range ($F > 0.5$); then, (35) is always true for $\beta < \pi(1 - F)$, where cosine term is negative; otherwise, it is verified on the condition that

$$\lambda U_g < \lambda_0 = \frac{\sin\frac{\pi}{2F}}{\sin\frac{\beta}{2F}\cos\frac{\pi-\beta}{2F}}. \tag{36}$$

Similarly, (34b) forces the normalized voltage U_g to be

$$\lambda U_g < -\lambda_0 \tag{37}$$

in the semiplane $\beta < \pi(1 - F)$ only.
For $F > 1$, (34a) and (34b) are always verified, while the upper limit of (34c) returns (36) again.
Another constraint comes from (30) substituting (31a) into (28b) giving the following inequality in the whole interested range:

$$\lambda U_g > \lambda_1 = \frac{1}{\sin\frac{\beta}{2F}}. \tag{38}$$

Now, all these constraints must coexist in the (F, β) plane, as depicted in Fig. 8: (36) and (38) admit common solution if and only if $\lambda_0 > \lambda_1$, which is true for $F > 1$ with $\beta < \pi(2 - F)$ (Region I-a), and for $0.5 < F < 1$ with $\beta < \pi F$ (Region I-b); (37) and (38) are simultaneously true if only if $-\lambda_0 > \lambda_1$ that implies $\beta > \pi(2 - 3F)$ (Region II).
The λ_i functions correspond to the normalized voltage λU_g at the frontiers between different operating modes. In the considered range, the IBCI converter presents three voltage boundaries $\lambda_{0,1,2}$, reported in Table IV, in addition to $\lambda U_g = 1$ that corresponds to the limit of positive power flow condition, i.e., $V_A \geq V_B$.

5) *Find the normalized output power and the voltage conversion ratio* applying (24) and (26). For the CCM$_1$ mode, substituting in (24) the value of φ_1 given in (32), the

TABLE IV
VOLTAGE AND POWER MODE BOUNDARIES DEFINITIONS OF λU_g AND Γ

i	λ_i	Γ_i
0	$\frac{\sin\frac{\pi}{2F}}{\sin\frac{\beta}{2F}\cos\frac{\pi-\beta}{2F}}$	$\frac{2FG^2}{\pi}\left\lvert\tan\frac{\pi}{2F}\right\rvert\tan\frac{\pi-\beta}{2F}$
1	$\frac{1}{\sin\frac{\beta}{2F}}$	$\frac{2FG^2}{\pi}$
2	$\frac{1}{\cos\frac{\pi-\beta}{2F}}$	$\frac{2FG^2}{\pi}\left[1+\frac{1}{\cos\frac{\pi-\beta}{2F}}\right]$

TABLE V
CCM REGIONS AND $\lambda U_g/\Gamma$ BOUNDARIES

CCM	Normalized boundaries			
	Region	(F,β) plane	Voltage λU_g	Power Γ
0		$F>1$	$\lambda U_g>\lambda_0$	$\Gamma>\Gamma_0$
1	I	$\begin{cases}\beta<\pi F\\ \beta>\pi(1-F)\\ \beta<\pi(2-F)\end{cases}$	$\lambda_1<\lambda U_g<\lambda_0$	
	II	$\begin{cases}\beta<\pi(1-F)\\ \beta>\pi(2-3F)\end{cases}$	$\lambda_1<\lambda U_g<-\lambda_0$	$\Gamma_1<\Gamma<\Gamma_0$
2	I	$\begin{cases}\beta>\pi(1-F)\\ \beta>\pi(2F-1)\end{cases}$	$\lambda U_g>\lambda_2$	$\Gamma>\Gamma_2$
	II	$\begin{cases}\beta>\pi(1-F)\\ \beta<\pi(2F-1)\end{cases}$	$\lambda U_g>\lambda_0$	$\Gamma>\Gamma_0$

normalized power in function of U_g is obtained as

$$\Gamma=\frac{2FG^2}{\pi}\lambda U_g\,\frac{\sin\frac{\beta}{2F}}{\left\lvert\cos\frac{\pi}{2F}\right\rvert}\sqrt{1-\left(\frac{1}{\lambda U_g}\frac{\sin\frac{\pi}{2F}}{\sin\frac{\beta}{2F}}\right)^2}. \tag{39}$$

Substituting the voltage boundary values $\lambda_{0,1}$ into (39), the corresponding power boundaries values $\Gamma_{0,1}$ are found. At every λ_i, its Γ_i value is associated, as reported in Table IV. Using (26) and remembering that $U_g=M^{-1}$, the explicit value of the conversion ratio is found as

$$M=\frac{2FG^2\rho_o}{\pi}\lambda\,\frac{\sin\frac{\beta}{2F}}{\left\lvert\cos\frac{\pi}{2F}\right\rvert}\frac{1}{\sqrt{1+\left(\frac{2FG^2\rho_o}{\pi}\tan\frac{\pi}{2F}\right)^2}}. \tag{40}$$

Iterating this presented procedure for all the modes depicted in Fig. 7, the different regions in the (F,β) plane and normalized frontiers of λU_g and Γ are figured out and reported in Tables V and VI for the CCM and the DCM, respectively. In Table VII, the expressions of normalized power and unknown angles (φ for the CCM and α for the DCM) are summarized.

The DCM_2 mode, which is the resonant mode mostly exploited in the literature (see [29]– [32]), deserves a particular discussion because $\beta>\pi F$ and $\mathbf{W}'$ and $\mathbf{S}'$ become meaningless, thus simplifying the analysis compared to the other operating modes. In this mode, the converter behaves like a voltage source, since its voltage gain $M=\lambda$ is independent of the load,

TABLE VI
DCM REGIONS AND $\lambda U_g/\Gamma$ BOUNDARIES

DCM	Normalized boundaries			
	Region	(F,β) plane	Voltage λU_g	Power Γ
0	I	$\begin{cases}\beta<\pi F\\ \beta<\pi(2-F)\end{cases}$	$1<\lambda U_g<\lambda_1$	$\Gamma<\Gamma_1$
	II	$\beta>\pi(2-F)$	$1<\lambda U_g<\lambda_0$	$\Gamma<\Gamma_0$
1	I	$\beta>\pi F$	$1<\lambda U_g<\lambda_2$	$\Gamma_1<\Gamma<\Gamma_2$
	II	$\begin{cases}\beta<\pi F\\ \beta>\pi(1-F)\\ \beta>\pi(2F-1)\end{cases}$	$\lambda_0<\lambda U_g<\lambda_2$	$\Gamma_0<\Gamma<\Gamma_2$
2		$\beta>\pi F$	$\lambda U_g=1$	$\Gamma<\Gamma_1$

as easily obtained from (3). Applying (29) both at the end of the resonant semiperiod and at the falling edge of v_A, the condition $-F<U_0<0$ is obtained, and substituting it into (25), the power boundary $\Gamma<\Gamma_1$ is achieved (see Tables VI and VII).

As a final comment, it is worth mentioning that the presented analysis, as stated in the introduction, can be immediately extended to the voltage-fed counterpart topologies just making the input parameter λ independent of control variable and setting $\lambda\in\{0.5,1\}$ in case of half- or full-bridge usage, respectively. It is also useful to highlight that the nonresonant behavior can be simply obtained assuming $F\gg 1$.

C. Simulations and Experimental Verification

In order to test and validate the theoretical analysis presented in the previous paragraphs, simulations and measurements of a 95% efficient 300-W rated prototype have been done. The power stage was assembled with the International Rectifier *IRLS4030* and *AUIRLR3110Z* indicated with $S_{a,bL}$ and $S_{a,bH}$ in Fig. 6, respectively. The coupled inductors were made with two RM10 cores employing 3F3 ferrite material, on which six turns of 270×71 μm Litz wire (primary windings) and 24 turns of 35×100 μm Litz wire (secondary windings) were wound. Since each real mutual inductor presents both primary- and secondary-side leakage inductances, called $L_\lambda^{p/s}$, and magnetizing inductance, L_ϕ, to make it compatible with the used model of Fig. 6, the following transformations were used

$$L_m=L_\lambda^p+L_\phi \tag{41a}$$

$$L=2\left[L_\lambda^s+\frac{L_\lambda^pL_\phi}{n^2(L_\lambda^p+L_\phi)}\right] \tag{41b}$$

$$n=\left(1+\frac{L_\lambda^p}{L_\phi}\right)\frac{n_p}{n_s} \tag{41c}$$

where L represents the total energy transfer inductance of the resonant tank. By means of these transformations, the effect of a nonperfect magnetic coupling in the mutual inductors is captured in the model. All prototype parameters are summarized in Table VIII. A PLECS/Simulink model was employed to check the correspondence between the operating mode domains and their boundaries. In Fig. 9, the outcome of this study for

TABLE VII
CLOSED-FORM EXPRESSIONS OF NORMALIZED POWER Γ AND UNKNOWN ANGLES φ_i, α_i FOR CCM$_i$ AND DCM$_i$ MODES, RESPECTIVELY

Mode	Normalized output power Γ	Typical angle φ_i/α_i
CCM$_0$	$\frac{2FG^2}{\pi}\lambda U_g\left[-1+\frac{\cos\frac{\pi-\beta}{2F}}{\cos\frac{\pi}{2F}}\sqrt{1-\sin^2\frac{\beta-2\varphi_0}{2F}}\right]$	$\varphi_0=\frac{\beta}{2}-F\arcsin\left(\frac{1}{\lambda U_g}\frac{\sin\frac{\pi}{2F}}{\cos\frac{\pi-\beta}{2F}}\right)$
CCM$_1$	$\frac{2FG^2}{\pi}\lambda U_g\frac{\sin\frac{\beta}{2F}}{\left\lvert\cos\frac{\pi}{2F}\right\rvert}\sqrt{1-\cos^2\frac{\pi-\beta-2\varphi_1}{2F}}$	$\varphi_1=\frac{\pi-\beta}{2}\mp F\arccos\left(\frac{1}{\lambda U_g}\frac{\sin\frac{\pi}{2F}}{\sin\frac{\beta}{2F}}\right)$
CCM$_2$	$\frac{2FG^2}{\pi}\lambda U_g\left[1-\frac{\cos\frac{\pi-\beta}{2F}}{\cos\frac{\pi}{2F}}\sqrt{1-\sin^2\frac{\beta-2\varphi_2}{2F}}\right]$	$\varphi_2=\frac{\beta}{2}-F\arcsin\left(\frac{1}{\lambda U_g}\frac{\sin\frac{\pi}{2F}}{\cos\frac{\pi-\beta}{2F}}\right)$
DCM$_0$	$\frac{2FG^2}{\pi}\lambda U_g\frac{(\lambda U_g-1)\sin^2\frac{\beta}{2F}}{1-\lambda U_g\sin^2\frac{\beta}{2F}}$	$\alpha_0=\pi-2F\arctan\left(\frac{\lambda U_g\sin\frac{\beta}{2F}\cos\frac{\beta}{2F}}{1-\lambda U_g\sin^2\frac{\beta}{2F}}\right)$
DCM$_1$	$\frac{2FG^2}{\pi}\lambda U_g\frac{\sin^2\frac{\pi-\beta}{2F}}{1-\lambda U_g\cos^2\frac{\pi-\beta}{2F}}$	$\alpha_1=\pi(1-2F)+2F\arctan\left(\frac{\lambda U_g\sin\frac{\beta}{2F}\cos\frac{\beta}{2F}}{1-\lambda U_g\cos^2\frac{\beta}{2F}}\right)$
DCM$_2$	$\forall\Gamma:\lambda U_g=1$	$\alpha_2=\pi(1-F)$

TABLE VIII
PROTOTYPE PARAMETERS

Parameter	Symbol	Value	
Input voltage	V_g	15	V
Switching frequency	f_{sw}	185	kHz
Energy transfer capacitance	C	6.8(+33)	nF
Energy transfer inductance	L	55.6	μH
Magnetizing inductance	L_m	20	μH
Turn ratio	n_p/n_s	6/24	
Effective turn ratio	n	0.2644	
Clamp capacitors	C_{CL}	470 + 22	nF
Output capacitors	$C_{1,2}$	470	nF

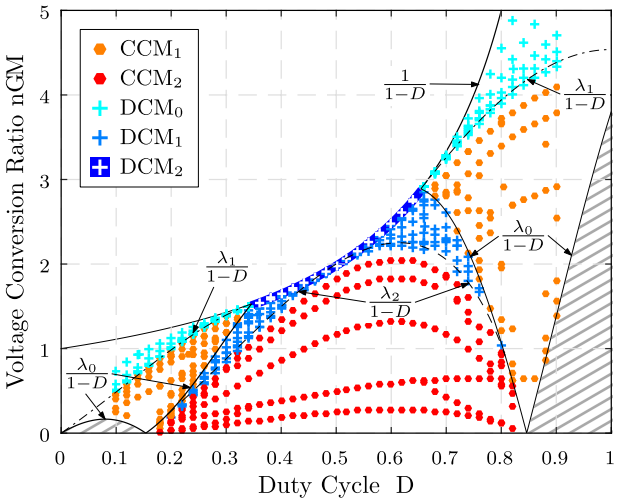

Fig. 9. Operating points obtained via simulation for different values of duty cycle D and load R_o at $F=0.71$. The colored dots indicate the operating mode to compare to the regions picked out with the analysis.

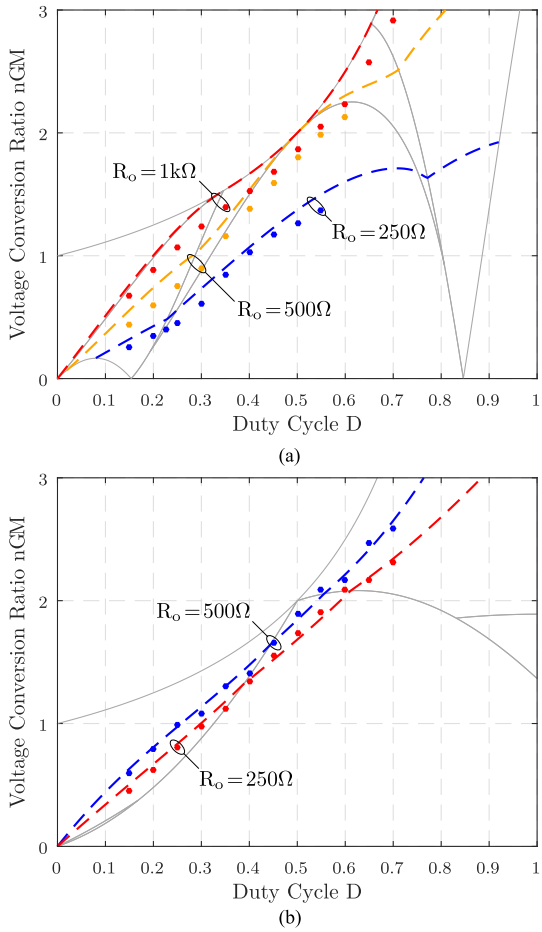

Fig. 10. Comparison between theoretical and experimental voltage conversion ratio nFM for different values of resonant frequency: experimental measurements are indicated with dots, while theoretical and voltage ratio are indicated with dashed lines. (a) $F=0.71$ ($C=6.8$ nF). (b) $F=1.73$($C=39.8$ nF).

$F=0.71$ is reported. The frontiers are well detected with the boundaries provided in Tables V and VI giving proof of the analysis. The prototype was used to measure the voltage gain nGM and compare it with the theoretical function (26) solution. In Fig. 10, different operating points, varying duty cycle and load, for two resonance frequencies are captured: the dots represent the prototype measurements, while the dashed lines the theoretical voltage gain. At first sight, the experimental values sketch a scaled version of the respective analytic solutions. To confirm this hypothesis, the sample Pearson correlation coefficient r has been calculated for each load configuration, and it appears always greater than 0.997. Since $r\simeq 1$, the real voltage gain M could be expressed by a linear function of the theoretical one

M_t. It is worth noting that the coefficient r value increases when it is calculated between M and ηM_t, where η is the measured efficiency, probably meaning that the linear dependence is a function of the efficiency.

V. Conclusion

In this paper, a general approach to solve the steady-state operation of the SR converter class has been proposed. The analytic solution for the sampled trajectory of current and voltage in the resonant tank at the commutation instants is provided, as well as the closed-form expression of the transferred power and the voltage conversion ratio. The normalized matrix representation allows a fast and flexible computation tool too.

The PSM DHB converter is studied with both the proposed method and the FHA approach to compare the error estimation of the inductor current at the switching instants and the transferred power.

The theoretical framework is proved by means of simulations and experimental measurements on a 300-W IBCI converter prototype. In addition to that, a comprehensive analysis of the IBCI converter is reported with a step-by-step guideline for the CCM and the DCM.

References

[1] I. Jitaru, "A 3 kw soft switching DC-DC converter," in *Proc. IEEE 15th Annu. Appl. Power Electron. Conf. Expo.*, 2000, vol. 1, pp. 86–92.

[2] F. Krismer and J. Kolar, "Closed form solution for minimum conduction loss modulation of dab converters," *IEEE Trans. Power Electron.*, vol. 27, no. 1, pp. 174–188, Jan. 2012.

[3] H. Bai and C. Mi, "Eliminate reactive power and increase system efficiency of isolated bidirectional dual-active-bridge DC-DC converters using novel dual-phase-shift control," *IEEE Trans. Power Electron.*, vol. 23, no. 6, pp. 2905–2914, Nov. 2008.

[4] H. Bai and C. Mi, "Correction to "eliminate reactive power and increase system efficiency of isolated bidirectional dual-active-bridge DC-DC converters using novel dual-phase-shift control," [Nov 08 2905-2914]," *IEEE Trans. Power Electron.*, vol. 27, no. 9, pp. 4177–4177, Sep. 2012.

[5] L. Cao, K. Loo, and Y. Lai, "Output-impedance shaping of bidirectional dab DC-DC converter using double-proportional-integral feedback for near-ripple-free dc bus voltage regulation in renewable energy systems," *IEEE Trans. Power Electron.*, vol. 31, no. 3, pp. 2187–2199, Mar. 2016.

[6] W. Choi, K.-M. Rho, and B.-H. Cho, "Fundamental duty modulation of dual-active-bridge converter for wide-range operation," *IEEE Trans. Power Electron.*, vol. 31, no. 6, pp. 4048–4064, Jun. 2016.

[7] J. Everts, F. Krismer, J. Van den Keybus, J. Driesen, and J. Kolar, "Optimal ZVS modulation of single-phase single-stage bidirectional dab ac-dc converters," *IEEE Trans. Power Electron.*, vol. 29, no. 8, pp. 3954–3970, Aug. 2014.

[8] F. Krismer and J. Kolar, "Efficiency-optimized high-current dual active bridge converter for automotive applications," *IEEE Trans. Ind. Electron.*, vol. 59, no. 7, pp. 2745–2760, Jul. 2012.

[9] B. Farhangi and H. Toliyat, "Piecewise linear model for snubberless dual active bridge commutation," *IEEE Trans. Ind. Appl.*, vol. 51, no. 5, pp. 4072–4078, Sep. 2015.

[10] S. J. Jang, C. Y. Won, B. K. Lee, and J. Hur, "Fuel cell generation system with a new active clamping current-fed half-bridge converter," *IEEE Trans. Energy Convers.*, vol. 22, no. 2, pp. 332–340, Jun. 2007.

[11] G. Spiazzi and S. Buso, "Analysis of the interleaved isolated boost converter with coupled inductors," *IEEE Trans. Ind. Electron.*, vol. 62, no. 7, pp. 4481–4491, Jul. 2015.

[12] Y. Zhao, W. Li, Y. Deng, and X. He, "Analysis, design, and experimentation of an isolated ZVT boost converter with coupled inductors," *IEEE Trans. Power Electron.*, vol. 26, no. 2, pp. 541–550, Feb. 2011.

[13] W. Li, L. Fan, Y. Zhao, X. He, D. Xu, and B. Wu, "High-step-up and high-efficiency fuel-cell power-generation system with active-clamp flyback-forward converter," *IEEE Trans. Ind. Electron.*, vol. 59, no. 1, pp. 599–610, Jan. 2012.

[14] Y. Zhao, X. Xiang, W. Li, X. He, and C. Xia, "Advanced symmetrical voltage quadrupler rectifiers for high step-up and high output-voltage converters," *IEEE Trans. Power Electron.*, vol. 28, no. 4, pp. 1622–1631, Apr. 2013.

[15] W. Li, H. Wu, H. Yu, and X. He, "Isolated winding-coupled bidirectional ZVS converter with PWM plus phase-shift (PPS) control strategy," *IEEE Trans. Power Electron.*, vol. 26, no. 12, pp. 3560–3570, Dec. 2011.

[16] X. Sun, X. Wu, Y. Shen, X. Li, and Z. Lu, "A current-fed isolated bidirectional DC-DC converter," *IEEE Trans. Power Electron.*, vol. 32, no. 9, pp. 6882–6895, Sep. 2017.

[17] F. Z. Peng, H. Li, G.-J. Su, and J. S. Lawler, "A new ZVS bidirectional DC-DC converter for fuel cell and battery application," *IEEE Trans. Power Electron.*, vol. 19, no. 1, pp. 54–65, Jan. 2004.

[18] X. Li and A. K. S. Bhat, "Analysis and design of high-frequency isolated dual-bridge series resonant DC/DC converter," *IEEE Trans. Power Electron.*, vol. 25, no. 4, pp. 850–862, Apr. 2010.

[19] J. Kan, S. Xie, Y. Tang, and Y. Wu, "Voltage-fed dual active bridge bidirectional DC/DC converter with an immittance network," *IEEE Trans. Power Electron.*, vol. 29, no. 7, pp. 3582–3590, Jul. 2014.

[20] R. Twiname, D. Thrimawithana, U. Madawala, and C. Baguley, "A new resonant bidirectional DC-DC converter topology," *IEEE Trans. Power Electron.*, vol. 29, no. 9, pp. 4733–4740, Sep. 2014.

[21] A. A. Aboushady, K. H. Ahmed, S. J. Finney, and B. W. Williams, "Steady-state analysis of full-bridge series resonant converter with phase-shift and frequency control," in *Proc. 5th IET Int. Conf. Power Electron., Mach. Drives*, Apr. 2010, pp. 1–6.

[22] L. Corradini, D. Seltzer, D. Bloomquist, R. Zane, D. Maksimovic, and B. Jacobson, "Minimum current operation of bidirectional dual-bridge series resonant DC/DC converters," *IEEE Trans. Power Electron.*, vol. 27, no. 7, pp. 3266–3276, Jul. 2012.

[23] F. Martin Ibanez, J. Martin Echeverria, J. Vadillo, and L. Fontan, "A step-up bidirectional series resonant DC/DC converter using a continuous current mode," *IEEE Trans. Power Electron.*, vol. 30, no. 3, pp. 1393–1402, Mar. 2015.

[24] F. Ibanez, J. M. Echeverria, and L. Fontan, "Novel technique for bidirectional series-resonant DC/DC converter in discontinuous mode," *IET Power Electron.*, vol. 6, no. 5, pp. 1019–1028, May 2013.

[25] B. S. Nathan and V. Ramanarayanan, "Analysis, simulation and design of series resonant converter for high voltage applications," in *Proc. IEEE Int. Conf. Ind. Technol.*, Jan. 2000, vol. 1, pp. 688–693.

[26] A. Safaee, P. Jain, and A. Bakhshai, "Time-domain steady-state analysis of fixed-frequency series resonant converters with phase-shift modulation," in *Proc. IEEE Transp. Electrific. Conf. Expo.*, Jun. 2014, pp. 1–7.

[27] A. Safaee, M. Karimi-Ghartemani, P. K. Jain, and A. Bakhshai, "Time-domain analysis of a phase-shift-modulated series resonant converter with an adaptive passive auxiliary circuit," *IEEE Trans. Power Electron.*, vol. 31, no. 11, pp. 7714–7734, Nov. 2016.

[28] F. M. Ibanez, J. M. Echeverria, J. Vadillo, and L. Fontan, "State-plane analysis of anomalous step-up behavior in series-resonant converters," *IEEE J. Emerg. Sel. Topics Power Electron.*, vol. 4, no. 3, pp. 1026–1035, Sep. 2016.

[29] J.-M. Kwon and B.-H. Kwon, "High step-up active-clamp converter with input-current doubler and output-voltage doubler for fuel cell power systems," *IEEE Trans. Power Electron.*, vol. 24, no. 1, pp. 108–115, Jan. 2009.

[30] J.-M. Kwon, K. Eung-Ho, B.-H. Kwon, and K.-H. Nam, "High-efficiency fuel cell power conditioning system with input current ripple reduction," *IEEE Trans. Ind. Electron.*, vol. 56, no. 3, pp. 826–834, Mar. 2009.

[31] G. Spiazzi, F. Sichirollo, and F. Goncalves, "Efficiency analysis of an isolated high voltage gain converter operating in resonant and non-resonant mode," in *Proc. IEEE Energy Convers. Congr. Expo.*, Sep. 2012, pp. 3875–3881.

[32] J. Hiltunen, V. Visnen, and P. Silventoinen, "A bidirectional current-fed resonant push-pull converter for low voltage, high current applications," in *Proc. IEEE Energy Convers. Congr. Expo.*, Sep. 2013, pp. 4770–4774.

[33] Y. Li, Y. Xing, Y. Lu, H. Wu, and P. Xu, "Performance analysis of a current-fed bidirectional LLC resonant converter," in *Proc. 42nd Annu. Conf. IEEE Ind. Electron. Soc.*, Oct. 2016, pp. 2486–2491.

[34] R. L. Steigerwald, "A comparison of half-bridge resonant converter topologies," in *Proc. 2nd IEEE Appl. Power Electron. Conf. Expo.*, Mar. 1987, pp. 135–144.

[35] G. Spiazzi, S. Buso, and D. Biadene, "Efficient high step-up topology for renewable energy source interfacing," in *Proc. IEEE Appl. Power Electron. Conf. Expo.*, Mar. 2015, pp. 1137–1144.

Davide Biadene (S'11) received the M.S. degree in electronic engineering from the University of Padua, Padua, Italy, in 2014, where he is currently working toward the Ph.D. degree at the Graduate School of Information Engineering, Department of Information Engineering.

He was a visiting Ph.D. student with the Power Electronic Systems Laboratory, Department of Information Technology and Electrical Engineering, ETH Zurich, Zurich, Switzerland, in 2016. His current research interests include dc–dc converters for renewables and energy storage devices.

Giorgio Spiazzi (S'92–M'95) received the Graduate degree (*cum laude*) in electronic engineering and the Ph.D. degree in industrial electronics and informatics from the University of Padova, Padova, Italy, in 1988 and 1993, respectively.

He is currently an Associate Professor with the Department of Information Engineering, University of Padova. His main research interests include dc–dc converters for renewable energy sources, soft-switching techniques, solid-state lamp ballasts, and electromagnetic compatibility in power electronics.